

Structure-property relations of silicon oxycarbides studied using a machine learning interatomic potential

Niklas Leimeroth^{1,*}, Jochen Rohrer¹, and Karsten Albe¹

¹Institut für Materialwissenschaft, Technische Universität Darmstadt,
Otto-Berndt-Strasse 3, 64287 Darmstadt, Germany

*Corresponding author email: leimeroth@mm.tu-darmstadt.de

March 18, 2024

Abstract

Silicon oxycarbides show outstanding versatility due to their highly tunable composition and microstructure. Consequently, a key challenge is a thorough knowledge of structure-property relations in the system. In this work, we fit an atomic cluster expansion potential to a set of actively learned DFT training data spanning a wide configurational space. We demonstrate the ability of the potential to produce realistic amorphous structures and rationalize the formation of different morphologies of the turbostratic free carbon phase. Finally, we relate the materials stiffness to its composition and microstructure, finding a delicate dependence on Si-C bonds that contradicts commonly assumed relations to the free carbon phase.

1 Introduction

Silicon oxycarbides (Si-O-Cs) are highly versatile materials that combine remarkable structural and functional properties. Among them are high temperature resistance, good mechanical strength [1, 2], great creep- and corrosion-resistance [3, 4], as well as piezoresistivity and the ability to reversibly store Li^+ , Na^+ and K^+ [5, 6, 7, 8]. These properties make them interesting for applications in very different fields, such as protective coatings [9], energy storage [10] and biomedicine [11].

Despite the plethora of desirable properties and intensive research, open questions about structural features and their relation even to basic characteristics such as the Young's modulus (E) remain. From NMR measurements it is known that Si-O-Cs consist of corner-shared $\text{SiO}_x\text{C}_{4-x}$ tetrahedra with car-

bidic sp^3 -hybridized carbon [12, 13] and a segregated secondary phase with sp^2 -hybridized turbostratic carbon [14, 15]. The detailed nanostructure, however, remains elusive and sensitively depends on the composition, precursor structure and processing conditions. For example, it is still unclear in which form the turbostratic carbon is present in Si-O-C. Scarmi et al. [16] and Saha et al. [17] argued that interpenetrating networks of graphene-like carbon and silica-rich mixed tetrahedra domains are formed, based on the high creep resistance of the material. In contrast, Widjeon et al. [12] found that a model with graphitic inclusions embedded in a silica rich matrix result in a better match of the mass fractal dimensions of mixed tetrahedra.

Here, atomistic simulations may help in understanding structure formation and structure-property relations of Si-O-C compounds at the nanoscale. As shown for example in a series of studies by Kroll [18, 19, 20], ab-initio molecular dynamics (MD) simulations can be employed to investigate structural details, energetics and elastic properties of Si-O-C, but are limited to structures consisting of a few hundred atoms and simulation times on the order of tens of picoseconds. Consequently, the heterogeneity on the nanoscale intrinsic to Si-O-C can not be reproduced in full extend. Large-scale MD simulations, on the other hand, require suitable interatomic potentials and the complex nature of the strongly directional covalent bonds is hard to capture in empirical formulas like bond order potentials. Recent studies showed that the ReaxFF framework [21] allows to study specific aspects of the Si-O-C system. For example, Newsome et al. simulated the oxidation of silicon car-

bide [22]. Soria et al. investigated organic molecules on silicon surfaces [23], Gao et al. and Ponomarev et al. simulated the pyrolysis of specific polymers to amorphous Si-O-C [24, 25]. These potentials, however, have a limited scope and require a reparametrization for each application. Furthermore, only two out of the four parameter sets are publicly available [22, 23]. Here, modern machine learning interatomic potentials (MLIPs) offer an alternative approach to describe complex systems over a wide compositional and structural range at similar computational cost, but at the expense of requiring more training data. Recent studies have shown the successful application of MLIPs to carbon [26, 27, 28, 29, 30, 31, 32, 33], silicon [34, 35, 36, 37, 38, 39], SiO₂ [40, 41, 42, 43] and SiC [44, 45]. In this work, we present an Atomic Cluster Expansion (ACE) potential for the Si-O-C system fitted to an extensive database generated using the active learning (AL) capabilities of Moment Tensor potentials (MTPs) [46] and ACE [47]. We show that the potential achieves a high accuracy for a wide compositional range and that it can be used to produce realistic amorphous Si-O-C structures. We investigate structural features, formation energies and Young’s moduli for samples with varying compositions and precursor configurations. Thereby, we find that the structure model containing graphene like sheets and the graphitic inclusions in a silica matrix are both likely to describe the structure of Si-O-C, but occur at different stages of processing. Furthermore, we establish relations of Young’s modulus to the fraction of Si-C bonds in mixed SiO_xC_{4-x} tetrahedra and the silica volume.

2 Methods

2.1 Training and testing data

The training data for the potential was produced as follows. Initial Si, O and Si-O structures were taken from an ACE potential previously fitted for the Si-O system [48]. Pure C structures were generated using the ASE package [49] and SiC structures were taken from the materials project database [50]. Si-O-C structures with varying compositions were generated with two different procedures. Firstly, structures were produced to match the expected coordination, i.e. 4-fold

	X _{Si}	X _O	X _C
Si ₂ O ₂ C	0.4	0.4	0.2
PMSQ	0.25	0.5	0.25
RD-212	0.25	0.25	0.5
SILRES-604	0.125	0.125	0.75
RD-684	≈0.121	≈0.121	≈0.758

Table 1: Compositions of hydrogen stripped polymers, sorted from low to high carbon content. These compositions were used to generate polymer derived (PD), bulk fragment (BF), isolated atoms (Ats) and graphite flakes and isolated atoms (GrAts) samples (See Fig. 1a).

for Si and C and 2-fold for O [51, 52]. Additional structures were then generated using an AL procedure, schematically shown in Fig. 1. We employed PACKMOL [53], which implements an algorithm to densely pack structural fragments while keeping adjustable minimal distances between atoms [54]. With this approach structures based on polymers inspired from Polymethylsilsesquioxane (PMSQ), the polyorganosiloxanes RD-212, RD-684 and SILRES-604 and a fully artificial polymer made from Si₂O₂C monomers were generated with removed H atoms. In the following we will use the compositions, instead of polymer names as shown in Tab. 1. Stripping H from the polymers avoids a massive extension of the necessary training data, as the configuration space for a quarternary system is much larger than for a ternary, but keeps the polymeric backbone. We expect that this has a negligible influence for final structures produced with pyrolysis temperatures of 1273 K to 1523 K and higher, because H evaporates during synthesis and the remaining amount of H atoms in them is very small [55, 56, 57].

In order to cover a wider variety of compositions and structural features, we also produced configurations made from isolated atoms (Ats) and bulk fragments (BFs) SiO₂, SiC₄, CSi₄ and C₆ as shown in Fig. 1a. For the structures generated directly from Ats and BFs the composition was varied, with Si and C concentrations ranging from 0% to 100% and the oxygen concentration from 0 to 2.2 times the Si concentration. The AL capabilities of MTPs [58] and ACE potentials [47] were employed to iteratively generate new Si-O-C configurations

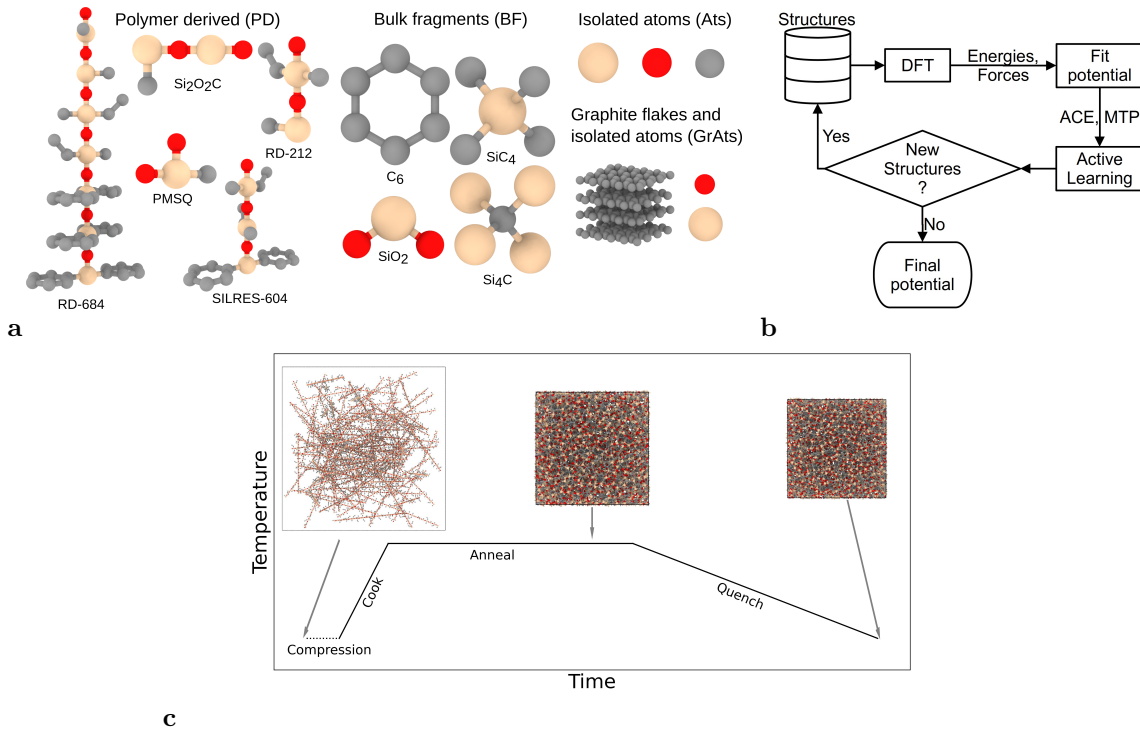


Figure 1: **Si-O-C structure generation and active-learning strategy.** Most initial structures for the AL process were generated by densely packing smaller building blocks using the PACKMOL program. These building blocks and the nomenclature used to describe them throughout this work are shown in (a). Si is shown in beige, O in red and C in gray. PD structures are stripped of H atoms. GrAts building blocks were used to produce large sample structures, but not in the AL process. The AL procedure employed to iteratively improve the training data is schematically shown in (b). Structures for AL and samples used in the analysis were produced using a cook and quench simulations depicted in (c). The compressions step shown as dotted line was only applied for PD and GrAts structures, where it was necessary to obtain nonporous bulk samples. For structures made from BF's or Ats it was not necessary, because the initial packing already leads to reasonable densities.

as shown in Fig. 1b. Here, we started with MTPs because the AL capabilities for ACE were implemented only recently [47]. Furthermore, we covered a wider variety of structures by using both codes. The training data set was considered complete when no new structures, that had a maximum density-functional theory (DFT) force of less than $150 \text{ eV}/\text{\AA}$, were discovered in cook and quench simulations with temperatures up to 3000 K and pressures up to 200 GPa.

For the test data set the test data of the Si-O potential [48] was supplemented with a separately created set of Si-O-C structures. These Si-O-C test structures were created with PACKMOL at varying densities and compositions. Consequently, the atoms were randomly displaced.

Finally, the training and test data sets were filtered to not contain structures with a maxi-

imum force of more than $150 \text{ eV}/\text{\AA}$, a minimal distance between atoms smaller than 0.6\AA or greater than 4\AA or an energy of more than $20 \text{ eV}/\text{atom}$ above the convex hull.

2.2 Details of potentials

For the potentials we used a cutoff of 5\AA . The ACE and MTPs were fitted using the *pacemaker* [39, 59] and MLIP packages [46]. For the AL process with MTPs a level 26 potential was employed. The intermediate ACE potentials for AL were fitted with the triple embedding $\rho_1^{0.5} + \rho_2^1 + \rho_3^2$ and a total of 2325 basis functions. In principle, the most straightforward way of increasing the accuracy of ACE potentials is to increase the number of basis functions. However, this considerably increases the computational cost [59]. Instead, we tested different embedding terms for the fi-

nal potential, which is computationally very cheap. Here, we found a highly nonlinear sum of expansions $\sum_i^n \phi_i^{\alpha_i}$ with $n = 10$ and exponents α_i 0.125, 0.25, 0.375, 0.5, 0.75, 0.875, 1, 1.25, 1.5 and 2 to result in the best testing errors.

2.3 SiOC sample structures

The structure samples used to analyze formation energies, structural features and elastic properties were produced in a cook and quench process, as schematically shown in Fig. 1c. Here we tested two different degrees of freedom, the influence of the composition and the effect of the precursor on the structure and properties of the final sample. The compositions of the structures correspond to the 5 polymeric compositions shown in Tab. 1. As precursors, we employed 4 different types of building blocks shown in Fig. 1a. The graphite sheets in GrAts structures consist of 160 atom 2-layer graphite. The resulting 20 structures were used in cook and quench simulations with annealing temperatures of 1000, 1500 and 2000 K to obtain a total of 60 sample structures. Here, the annealing time was 1 ns. As shown in the supplemental material (section S1) this time is sufficient to reach a steady state regarding different structural features. The employed quench rate was 1×10^{12} K/s. PD and GrAts based structures required an additional compression step before the cook and quench process to obtain nonporous initial structures. For this purpose, they were equilibrated at 500 K with an applied isotropic pressure of 10 GPa for 10 ps before heating them up to the annealing temperature.

2.4 Simulations

DFT calculations were carried out with the same settings as used for a silica potential previously fitted [43] to keep the training data consistent. The plane wave code VASP [60, 61, 62] with projector-augmented wave [63] pseudopotentials and the SCAN [64] meta-GGA exchange-correlation were employed with a plane-wave cutoff of 900 eV and a k-spacing of 0.23 \AA^{-1} . Classical MD simulations were carried out with LAMMPS [65], applying GPU accelerated KOKKOS versions where possible. If not otherwise noted an NPT ensemble with isotropic 0 Pa pressure, Nosé-Hoover thermo-

and barostats and a timestep of 1 fs were employed in the simulations.

3 Results

In the following we will start by shortly presenting the results of the applied AL procedure and evaluate the newly developed MLIP. Then we will discuss the structure of the produced Si-O-C samples based on their composition and precursors going from low to high C contents. Finally, we will relate structural features to the Young’s modulus of the samples.

3.1 Training and performance of the potential

The flexibility of the ACE formalism allows for an accurate description of highly complex materials, under the condition that similar atomic configurations have been part of the data used in their training procedure. In this work, an AL procedure was employed to ensure that the training data covers a large phase space volume. Here, we started with MTPs as implemented in the MLIP package [46], and continued with ACE potentials for which AL capabilities were implemented only recently [47]. We included structures with varying compositions and at high temperatures and pressures, as well as different defective structures that can form during MD simulations. This makes the potential applicable to a wide area of problems. Fig. 2a and 2b show the resulting distribution of the training data in terms of atomic energies and volumes.

The mostly actively learned Si-O-C structures are scattered widely in this 2D representation of phase space. The pure elements and SiC structures were mostly made by hand. In combination with less compositional degrees of freedom this leads to a comparatively narrow distribution for them. To prevent the occurrence of unphysically large forces on single atoms during MD simulations at high temperatures or pressures we found it helpful to add SiC structures with a high density, leading to a second area with aggregated SiC structures around 4 eV/atom above the convex hull.

Energies and forces predicted using the potential agree well with those calculated using DFT over the whole range of structures, as shown in the scatter plots in Fig. 2c and 2d. For

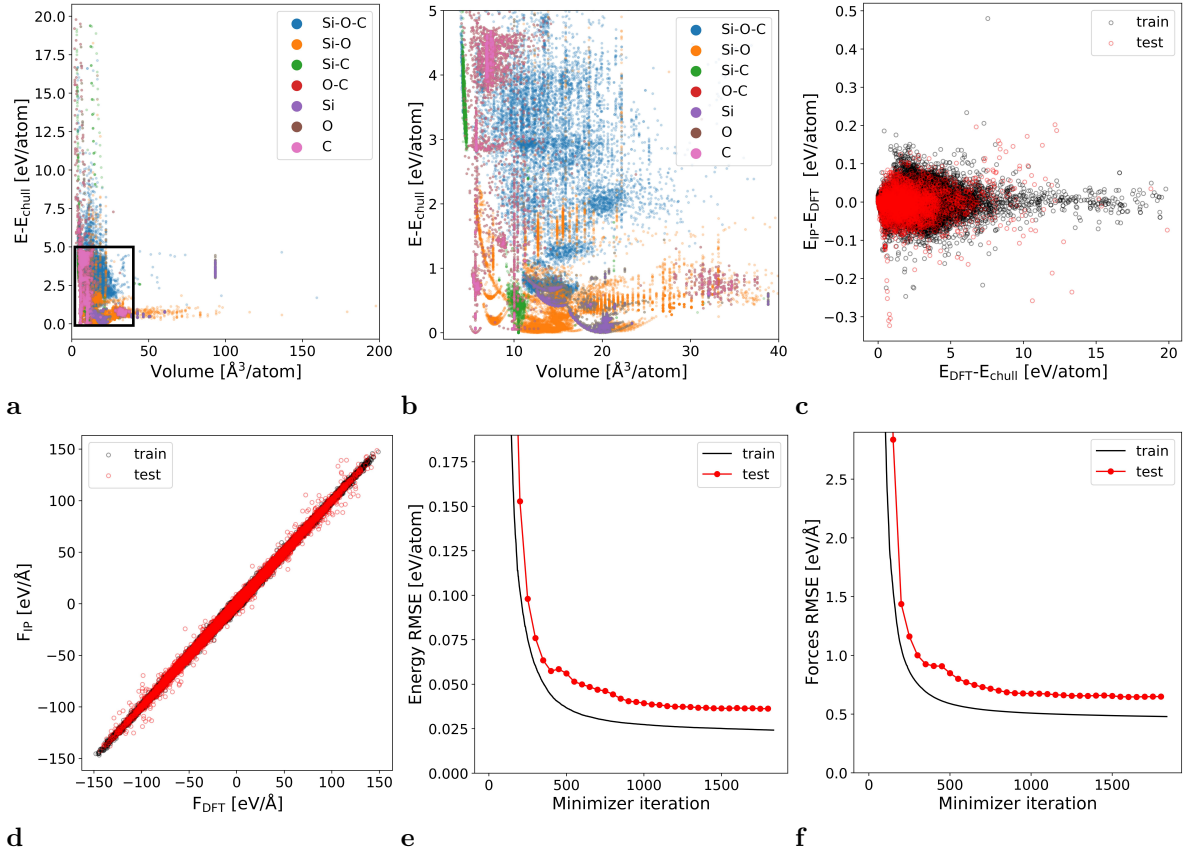


Figure 2: **Training data and performance of the potential.** Training data resulting from the AL procedure (a) with the black box indicating the magnified region shown in (b). Error of energies as function of the formation energy distance from the convex hull (c) and correlation of forces (d) as calculated with DFT and the ACE potential for the training and test datasets. Training and test RMSEs of energies (e) and forces (e) during optimization of the potential.

energies an RMSE of 24 and 36 meV/atom for the training and test sets were obtained. For forces the RMSEs were 479 and 650 meV/Å respectively. We want to note that the higher errors for the testing set are a result from the different distribution of the structures regarding their composition and energy and not from overfitting as shown by the continuous decrease of testing errors in Fig. 2e and 2f.

3.2 Structure and energetics

3.2.1 $\text{Si}_{0.4}\text{O}_{0.4}\text{C}_{0.2}$

The microstructure and properties of Si-O-C compounds depend strongly on the precursor material and processing conditions like pyrolysis temperature [7]. Time and lengths scales of the experimental processes can not be reproduced directly in MD simulations. Instead, we used different building blocks to produce a variety of microstructures in cook and quench simulations as previously described. Examples

of these initial structures are shown in the upper row of Fig. 3 Exemplary samples produced via the cook and quench protocol described in section 2.3 with an annealing temperature of 1500 K are shown in the row below. Qualitatively, the PD, BF and Ats structures are very similar. Major differences are only found for GrAts. Here, large graphite areas are still present in the final structure. From a purely thermodynamic viewpoint this is surprising, as one would expect that $\text{Si}_{0.4}\text{O}_{0.4}\text{C}_{0.2}$ decomposes into SiO_2 and SiC, but at the tested temperatures and timescales the kinetics do not allow for such a phase separation.

To quantify differences between the structures we calculated the Voronoi volume fractions occupied by 3-fold coordinated C atoms, i.e. the free carbon phase and SiO_4 tetrahedra, i.e. the silica phase. The results are shown in Fig. 4. Only the structures based on GrAts contain a meaningful amount of free carbon. As discussed previously there is no thermodynamic

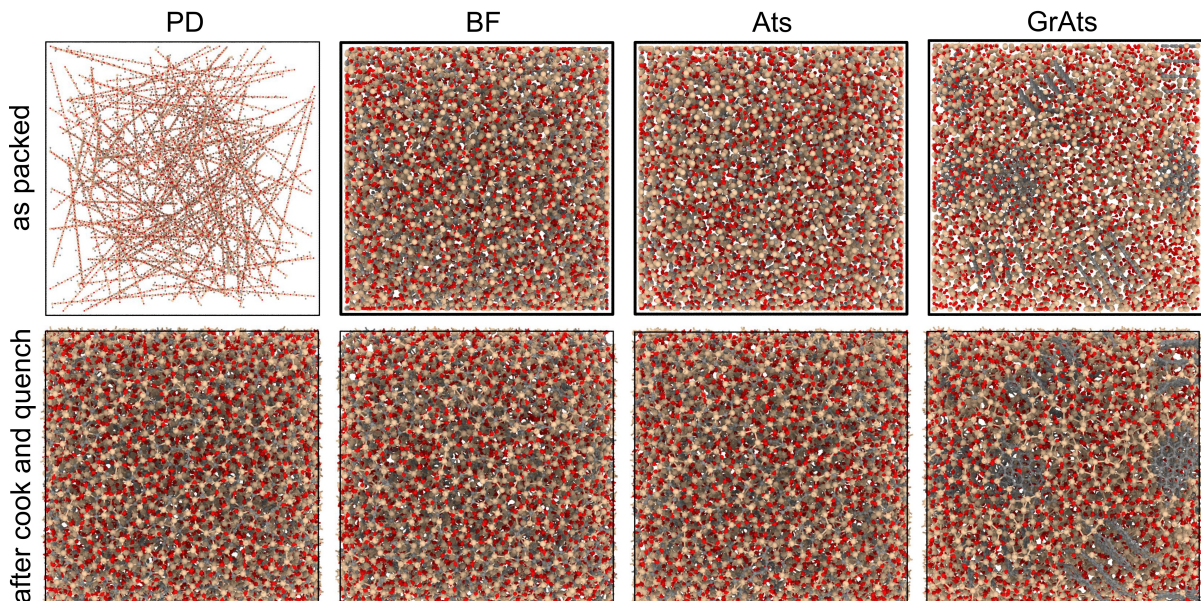


Figure 3: $\text{Si}_{0.4}\text{O}_{0.4}\text{C}_{0.2}$ assembled precursors and final structures. Shown are samples as packed with PACKMOL (upper row) and after the cook and quench process (lower row) with an annealing temperature of 1500 K for all structure prototypes. The PD, BF and Ats structures appear to be very similar upon visual inspection. The graphite like flakes in the GrAts based structure are still present after processing, showing that they are kinetically stabilized, as one would expect a decomposition into SiO_2 and SiC from an energetic viewpoint.

driving force for the formation of graphene or graphite like carbon, so its volume fraction is determined by the kinetics of the system and this behavior can be expected. In the GrAts structure the volume fraction stays constant between annealing temperatures 1000 and 1500 K. At 2000 K a slight decrease can be observed, showing that the graphite phase is kinetically stabilized up to Temperatures greater than 1500 K. Regarding the silica volume fraction a continuous increase at increasing temperatures can be observed for all structures, indicating a higher degree of phase separation. However, the data shows large differences with regard to the absolute values. The largest amount is observed for the GrAts structure, followed by BFs, Ats and finally the PD configuration. Again this observation can be rationalized by the thermodynamics and kinetics of the system. In the GrAts structure the unpaired Si and O atoms can quickly form silica without interference of the carbon, because it is already bound in the graphite phase. Si-C can only form in the relatively small interface regions or requires long range diffusion. In the BF based structure SiO_2 , SiC_4 and Si_4C units are already present, only requiring rotations and minor rearrangement to form the thermo-

dynamically favored products, while the diffusion paths necessary to achieve phase separation in the atom based structure are long and intermediate bonds can form and need to brake again. Similarly, the PD structure contains Si bonded to C and O, which needs to break before forming pure SiO_4 or SiC_4 tetrahedra. The right column of Fig. 4 shows the formation energy of samples with respect to α -quartz, β -SiC and graphite. In the case of $\text{Si}_{0.4}\text{O}_{0.4}\text{C}_{0.2}$ they are very close in energy, despite the significant structural differences. Especially for the structures annealed at 2000 K the difference of nearly 0 for may irritate, when considering that the system still contains a considerable amount of free carbon in the case GrAts, but this energetically unfavorable state is apparently compensated by the high fraction of very favorable silica in the system.

3.2.2 $\text{Si}_{0.25}\text{O}_{0.5}\text{C}_{0.25}$

The carbon content of $\text{Si}_{0.25}\text{O}_{0.5}\text{C}_{0.25}$ is very close to the previously discussed $\text{Si}_{0.4}\text{O}_{0.4}\text{C}_{0.2}$, but the different Si:O ratio leads to a different thermodynamic situation. In equilibrium $\text{Si}_{0.25}\text{O}_{0.5}\text{C}_{0.25}$ should split into a pure silica and a graphite phase, while no SiC

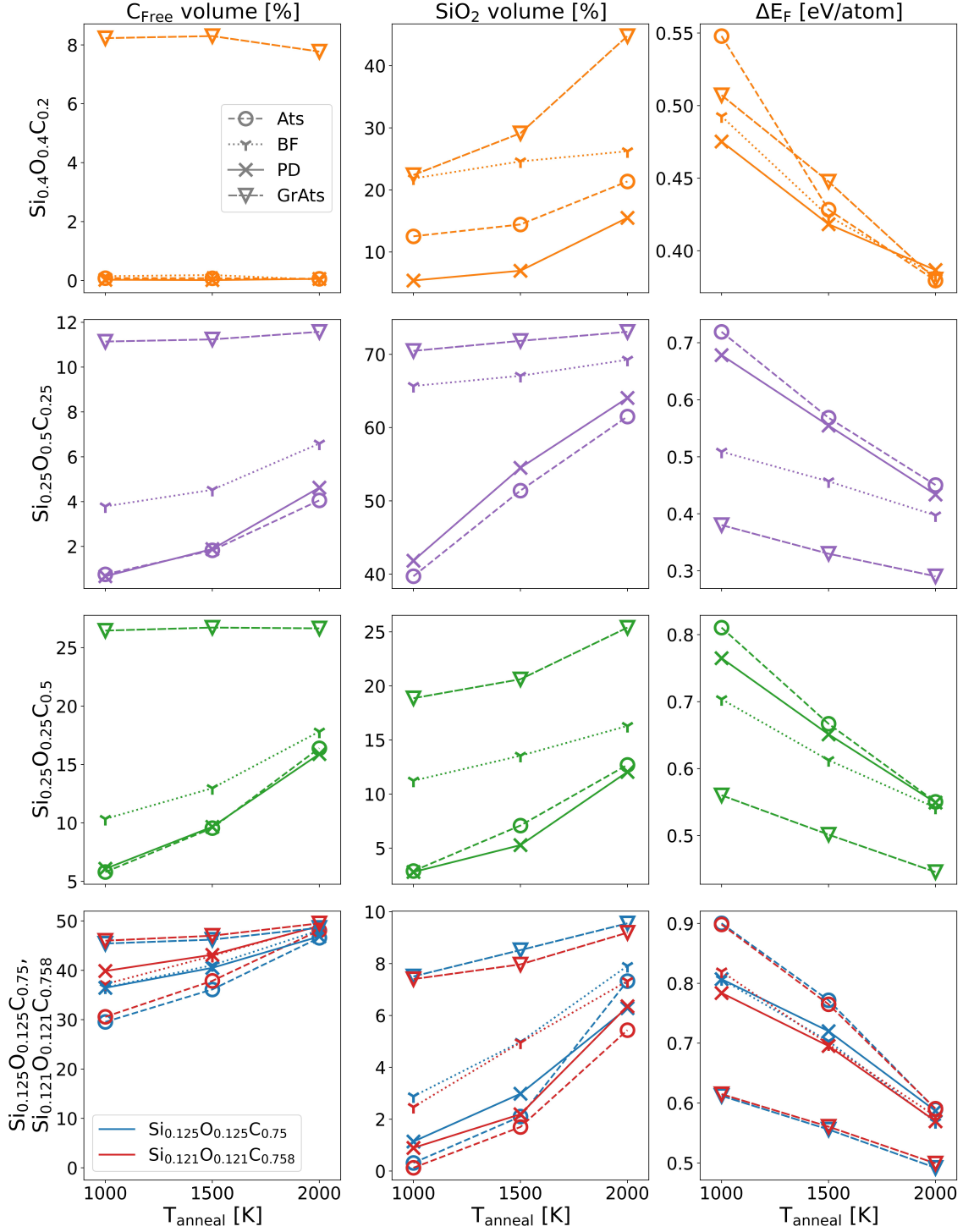


Figure 4: **Structure analysis and formation energies of Si-O-C samples.** The left column shows the free carbon volume fraction, defined as Voronoi volume of all 3-fold coordinated C atoms, the center column shows the silica volume fraction (Voronoi volume of SiO_4 tetrahedra). The right column contains the formation energies of samples with respect to α -quartz, β -SiC and graphite. Rows correspond to different sample compositions. $\text{Si}_{0.125}\text{O}_{0.125}\text{C}_{0.75}$ and $\text{Si}_{0.121}\text{O}_{0.121}\text{C}_{0.758}$ are shown in the same row, as a direct comparison of them is interesting especially in the case of PD structures due to their compositional similarity.

should form. Consequently, the formation energies of structures based on GrAts are considerably lower than those of the other precursors for $\text{Si}_{0.25}\text{O}_{0.5}\text{C}_{0.25}$. The difference between the Ats and GrAts structures with an annealing temperature of 1000 K is about 300 meV/atom, i.e. the driving forces for phase separation are very high. Since the structures are in a steady state, this also indicates a very low mobility. For an annealing temperature of 2000 K the difference between precursors becomes much smaller, reaching around 100 meV/atom. It is expected that the differences shrink, because the increased mobility at higher temperatures allows coming closer to the thermodynamic equilibrium. The free carbon and silica volume in $\text{Si}_{0.25}\text{O}_{0.5}\text{C}_{0.25}$ samples increases significantly with increasing annealing temperatures. The least changes are observed for the GrAts structure, which is already close to the phase separation. Generally, the arguments regarding the kinetics of the different precursors discussed for $\text{Si}_{0.4}\text{O}_{0.4}\text{C}_{0.2}$ also apply for $\text{Si}_{0.25}\text{O}_{0.5}\text{C}_{0.25}$, so similar trends can be observed, with the main differences determined by the decomposition products.

3.2.3 $\text{Si}_{0.25}\text{O}_{0.25}\text{C}_{0.5}$, $\text{Si}_{0.125}\text{O}_{0.125}\text{C}_{0.75}$ and $\text{Si}_{0.121}\text{O}_{0.121}\text{C}_{0.758}$

$\text{Si}_{0.25}\text{O}_{0.25}\text{C}_{0.5}$, $\text{Si}_{0.125}\text{O}_{0.125}\text{C}_{0.75}$ and $\text{Si}_{0.121}\text{O}_{0.121}\text{C}_{0.758}$ contain Si and O in a 1:1 ratio, but, in contrast to $\text{Si}_{0.4}\text{O}_{0.4}\text{C}_{0.2}$, also excess carbon. Thus we expect the formation of a varying amount of free carbon phase in the system and not just SiO_2 and SiC . The compositional similarity of $\text{Si}_{0.125}\text{O}_{0.125}\text{C}_{0.75}$ and $\text{Si}_{0.121}\text{O}_{0.121}\text{C}_{0.758}$ allows us to investigate the influence of different polymer-like precursor structures. In the $\text{Si}_{0.121}\text{O}_{0.121}\text{C}_{0.758}$ polymer C_6 rings are stacked very closely (cf. Fig. 1a), which could ease the formation of graphite. However, this can not be observed in our data. Generally the three compounds show high free carbon contents and qualitatively similar temperature dependence for both, the silica and free carbon fractions. The energetically most favorable sample is the one made from GrAts. Similar to $\text{Si}_{0.4}\text{O}_{0.4}\text{C}_{0.2}$ this can be explained by the high degree of phase separation, which corresponds to the thermodynamic equilibrium. $\text{Si}_{0.125}\text{O}_{0.125}\text{C}_{0.75}$ and $\text{Si}_{0.121}\text{O}_{0.121}\text{C}_{0.758}$ behave similar.

3.2.4 Relation to model structures

As discussed previously, two models for the nanostructure of Si-O-C exist. One suggests silica rich nanodomains, which are separated by an interconnected graphene like carbon network [16, 17]. The other describes the structure as graphitic inclusions in a silica rich matrix [12]. The results from our simulations are shown in Fig. 5. For structures that should contain graphite upon decomposition we found the GrAts models to be energetically favorable, favoring the latter model. However, in the other samples no graphitic carbon could be found and instead graphene like layers spread through the system, pointing to the former. This allows us to conclude that both models are representative for two distinct stages. In early stages of structure formation the structure is likely described by the first model, because the slow kinetics in the system prevent the formation of graphitic inclusions. With increasing temperatures and pyrolysis times the structure evolves towards the latter model argued for by Widgeon et al., as it is lower in energy.

3.3 Elastic properties

The structure of Si-O-C is highly tunable, depending on the pyrolysis conditions and precursors. An understanding of structure-property relations can therefore guide the search for processing routes that best match specific needs. Here, we investigate the structural features influencing the elastic properties of Si-O-C. For this purpose we calculated the elastic tensors of our samples using pymatgen [72] and derived the Young's modulus

$$E = \mu(3\lambda + 2\mu)/(\lambda + \mu) \quad (1)$$

with the Lamè constants $\mu = C_{44}$ and $\lambda = C_{12}$, as valid for isotropic materials. Here, the assumption of isotropy is very accurate with differences between C_{ij} that should be equivalent due to symmetry in the range of $\pm 3\%$. Only the GrAts structures show larger anisotropies, due to the limited amount of randomly orientated graphite flakes, leading to differences in the range of $\pm 15\%$. To reduce resulting errors we averaged over the supposedly equivalent directions. The deformations applied to obtain elastic tensors are not fully reversible because the relaxation of atomic positions leads to

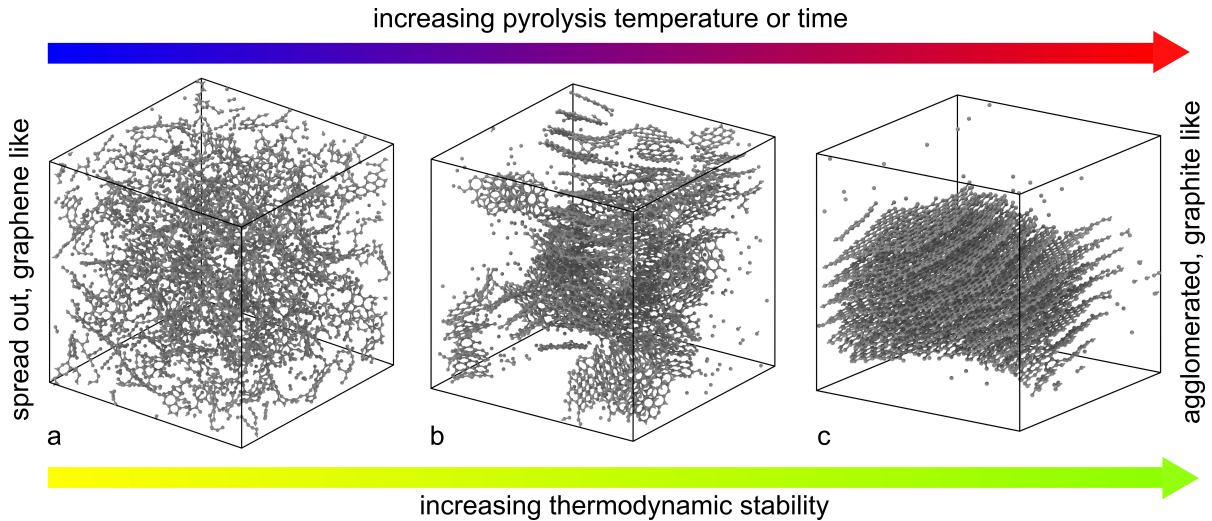


Figure 5: **Structure formation of free carbon phase in Si-O-C.** For low pyrolysis temperatures and times graphene like carbon forms as argued by Scarmi et al. [16] and Saha et al. [17] based on high creep resistance. At higher temperatures energetically more favorable graphite like agglomerates form, which are consistent with the mass fractal dimension as found by Widgeon et al. [12]. The figures show the free carbon phase as found for $\text{Si}_{0.25}\text{O}_{0.25}\text{C}_{0.5}$ PD sample annealed at 2000 K (a), GrAts sample annealed at 2000 K (b) and an additional PD sample annealed at 3500 K (c). Their formation energies suggests that the Si-O-C system would evolve from PD to GrAts structures, so we consider it as an intermediate step even though timescales accessible in MD do not allow a direct observation.

small energy barriers on the path back to the initial state that cannot be overcome in static relaxations. Corresponding energy-strain relations can be found in the supplemental material.

Fig. 6 shows the dependence of E on the SiO_4 volume, the average amount of carbon in $\text{SiO}_{4-x}\text{C}_x$ tetrahedra and the free carbon volume in the samples. Generally the modulus ranges from 70 GPa, which corresponds to E of silica glass [73] up to around 145 GPa, which agrees well with experiments. Also, it scatters significantly between different compositions and building blocks, showing the multidimensional nature of the problem. Strong correlations of E can be seen for the SiO_4 volume fraction and the amount of carbon within $\text{SiO}_{4-x}\text{C}_x$ tetrahedra. As expected the modulus decreases for higher silica volume fractions, approaching that of the pure amorphous phase and increases with an increasing amount of carbon in the mixed bonds. As discussed previously, GrAts based structures contain high amounts of SiO_4 tetrahedra and the C atoms are bound within the graphite inclusions, i.e. they do not participate much in mixed bonding. Consequently, these structures have lower Young's moduli than structures based on other

building blocks at the same compositions. Experimental studies have established empirical relations between structural features of Si-O-C and its elastic properties. Typically, it is observed that the Young's modulus increases with the amount of SiC and C within the $\text{SiO}_{4-x}\text{C}_x$ tetrahedra and decreases with increasing free carbon volume [67, 71]. However, as shown by Stabler et al. [70] the results can differ significantly based on the kind of sample and applied measurement method. Furthermore, a recent simulation based study by Haseen and Kroll [74] found a strong decrease of E with decreasing sample densities employing a Tersoff type potential. They argued that this could overlap the direct effect of the C_{free} phase, because the density of samples also strongly correlates with the amount of C_{free} . Indeed, they observed an increase of E with higher free carbon contents for samples with same density. These results fit well to our observation of a weak overall correlation of E with C_{free} . If anything, when taking into account all data points we observe a slight increase. Considering each composition individually can also help to resolve the discrepancy with experimental results, as all of them but $\text{Si}_{0.25}\text{O}_{0.5}\text{C}_{0.25}$ show downwards trends.

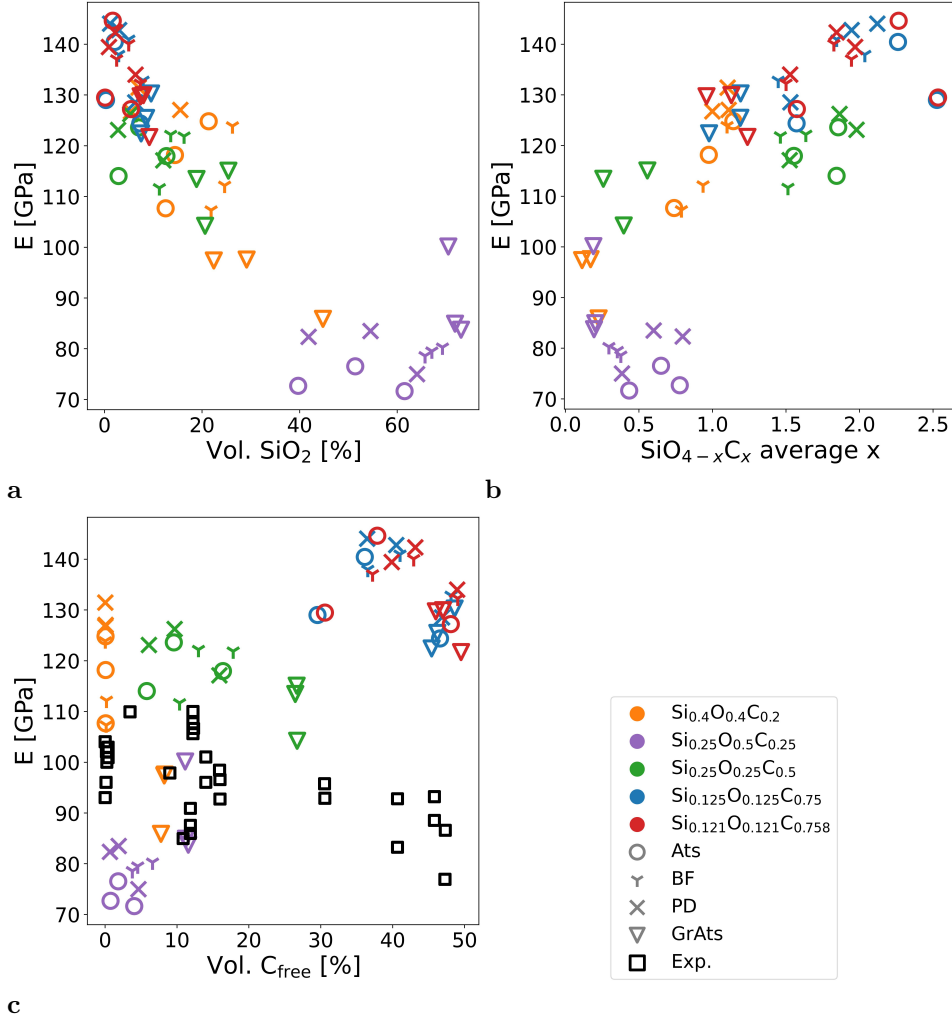


Figure 6: **Dependence of E on structural features.** Calculated E values for samples in dependence of silica volume fraction (**a**), average amount of carbon in mixed tetrahedra (**b**) and free carbon volume fraction (**c**). Experimental data in (**c**) is taken from [66, 67, 68, 69, 3, 70] as collected in [70] and from [71].

Therefore, we conclude that the amount of free carbon only weakly influences E, but at similar compositions more free carbon is equivalent to lower amounts of the strong Si-C bonds, indirectly leading to a lower stiffness.

4 Conclusion

Using multiple iterations of AL techniques implemented for MTPs and ACE potentials we produced a highly diverse set of amorphous Si-O-C structures, spanning a large area of phase space. With the converged dataset, we fitted a nonlinear ACE potential to energies and forces calculated with DFT and showed that the potential can accurately reproduce them. Due to the diversity of the training data, the potential has a large applicability

range and can describe the formation of Si-O-C compounds and their properties in a large temperature and pressure range.

Applying the potential, we produced amorphous Si-O-C samples with various compositions in a cook and quench procedure. Here, we tested the influence of different initial structures on the final configuration. We found that manually added graphite agglomerates are kinetically stabilized in MD simulation times and lead to energetically favorable states compared to graphene like sheets, if the structure contains excess C. However, their formation is kinetically hindered, and we assume that an interpenetrating network of silica rich domains and graphene like sheets is formed as an intermediate step during synthesis of amorphous Si-O-C.

To test and establish structure-property rela-

tions in Si-O-C we calculated Young's moduli of the samples. We found that the silica volume fraction and the average amount of carbon in mixed $\text{SiO}_{4-x}\text{C}_x$ tetrahedra correlate well with the stiffness across all samples. Silica reduces the stiffness and high amounts of Si-C bonds increase it. Furthermore, the free carbon volume fraction is a good indicator of E for samples with similar compositions, but not in general.

We believe that the presented potential will allow detailed investigations of structure formation and properties in Si-O-C. In a broader context, we have shown that modern MLIPs can be employed to study multi element material systems that form highly complex structures. Therefore, they can greatly benefit the understanding of glassy and ceramic materials on the atomistic scale.

Acknowledgments

N. L. acknowledges Linus C. Erhard for helpful discussions. N. L. received funding from the Deutsche Forschungsgemeinschaft (DFG, German Research Foundation) under grant number 405621137 and from the German Federal Ministry of Education and Research (BMBF) under project HeNa (FKZ 03XP0390A). J. R. acknowledges funding from the European Unions Horizon 2020 research and innovation programme under Grant Agreement no. 963542. K. A. acknowledges funding by the DFG under project number 413956820. The authors gratefully acknowledge the computing time provided to them on the high-performance computer Lichtenberg at the NHR Centers NHR4CES at TU Darmstadt. This is funded by the German Federal Ministry of Education and Research, and the state governments participating.

Data availability

The potential and datasets are available on zenodo upon journal acceptance [75].

Author contributions

N. L. performed most computations and analysis. J. R. provided hand crafted Si-O-C structures and performed early AL iterations with

MTPs. All authors contributed to the research design and interpretation of results. N. L. wrote the paper with input from J. R. and K. A.

Competing interests

The authors declare no competing interests.

References

1. Li Z, Chen Z, Liu J, Fu Y, Liu C, Wang P, Jiang M, and Lao C. Additive Manufacturing of Lightweight and High-Strength Polymer-Derived SiOC Ceramics. *Virtual and Physical Prototyping*. 2020 Apr 2; 15:163–77. DOI: 10.1080/17452759.2019.1710919
2. Barrios E and Zhai L. A Review of the Evolution of the Nanostructure of SiCN and SiOC Polymer Derived Ceramics and the Impact on Mechanical Properties. *Molecular Systems Design & Engineering*. 2020; 5:1606–41. DOI: 10.1039/D0ME00123F
3. Papendorf B, Ionescu E, Kleebe HJ, Linck C, Guillon O, Nonnenmacher K, and Riedel R. High-Temperature Creep Behavior of Dense SiOC-Based Ceramic Nanocomposites: Microstructural and Phase Composition Effects. *Journal of the American Ceramic Society*. 2013; 96:272–80. DOI: 10.1111/jace.12067
4. Stabler C, Roth F, Narisawa M, Schliephake D, Heilmaier M, Lauterbach S, Kleebe HJ, Riedel R, and Ionescu E. High-Temperature Creep Behavior of a SiOC Glass Ceramic Free of Segregated Carbon. *Journal of the European Ceramic Society*. Preparation and Application of Ultra-high Temperature Ceramic Matrix Composites 2016 Nov 1; 36:3747–53. DOI: 10.1016/j.jeurceramsoc.2016.04.015
5. Melzi d'Eril M, Zambotti A, Graczyk-Zajac M, Ionescu E, Sorarù GD, and Riedel R. Effect of Ultra-Fast Pyrolysis on Polymer-Derived SiOC Aerogels and Their Application as Anodes for Na-ion Batteries. *Open Ceramics*. 2023 Jun 1; 14:100354. DOI: 10.1016/j.oceram.2023.100354
6. Vallachira Warriam Sasikumar P, Zera E, Graczyk-Zajac M, Riedel R, and Soraru GD. Structural Design of Polymer-Derived SiOC Ceramic Aerogels for High-Rate Li Ion Storage Applications. *Journal of the American Ceramic Society*. 2016; 99:2977–83. DOI: 10.1111/jace.14323
7. Stabler C, Ionescu E, Graczyk-Zajac M, Gonzalo-Juan I, and Riedel R. Silicon Oxycarbide Glasses and Glass-Ceramics: "All-Rounder" Materials for Advanced Structural

- and Functional Applications. *Journal of the American Ceramic Society*. 2018 Nov; 101:4817–56. DOI: 10.1111/jace.15932
8. Chandra C, Devina W, Cahyadi HS, Kwak SK, and Kim J. Understanding Lithium, Sodium, and Potassium Storage Mechanisms in Silicon Oxycarbide. *Chemical Engineering Journal*. 2022 Jan 15; 428:131072. DOI: 10.1016/j.cej.2021.131072
 9. Lu K and Erb D. Polymer Derived Silicon Oxycarbide-Based Coatings. *International Materials Reviews*. 2018 Apr 3; 63:139–61. DOI: 10.1080/09506608.2017.1322247
 10. Wen Q, Qu F, Yu Z, Graczyk-Zajac M, Xiong X, and Riedel R. Si-Based Polymer-Derived Ceramics for Energy Conversion and Storage. *Journal of Advanced Ceramics*. 2022 Feb 1; 11:197–246. DOI: 10.1007/s40145-021-0562-2
 11. Arango-Ospina M, Xie F, Gonzalo-Juan I, Riedel R, Ionescu E, and Boccaccini AR. Review: Silicon Oxycarbide Based Materials for Biomedical Applications. *Applied Materials Today*. 2020 Mar 1; 18:100482. DOI: 10.1016/j.apmt.2019.100482
 12. Widgeon SJ, Sen S, Mera G, Ionescu E, Riedel R, and Navrotsky A. ²⁹Si and ¹³C Solid-State NMR Spectroscopic Study of Nanometer-Scale Structure and Mass Fractal Characteristics of Amorphous Polymer Derived Silicon Oxycarbide Ceramics. *Chemistry of Materials*. 2010 Dec 14; 22:6221–8. DOI: 10.1021/cm1021432
 13. Mera G, Navrotsky A, Sen S, Kleebe HJ, and Riedel R. Polymer -Derived SiCN and SiOC Ceramics – Structure and Energetics at the Nanoscale. *Journal of Materials Chemistry A*. 2013; 1:3826–36. DOI: 10.1039/C2TA00727D
 14. Sorarù GD, D’Andrea G, Campostrini R, Babonneau F, and Mariotto G. Structural Characterization and High-Temperature Behavior of Silicon Oxycarbide Glasses Prepared from Sol-Gel Precursors Containing Si-H Bonds. *Journal of the American Ceramic Society*. 1995; 78:379–87. DOI: 10.1111/j.1151-2916.1995.tb08811.x
 15. Roth F, Waleska P, Hess C, Ionescu E, and Nicoloso N. UV Raman Spectroscopy of Segregated Carbon in Silicon Oxycarbides. *Journal of the Ceramic Society of Japan*. 2016; 124:1042–5. DOI: 10.2109/jcersj2.16100
 16. Scarmi A, Sorarù G, and Raj R. The Role of Carbon in Unexpected Visco(an)Elastic Behavior of Amorphous Silicon Oxycarbide above 1273K. *Journal of Non-Crystalline Solids*. 2005 Aug; 351:2238–43. DOI: 10.1016/j.jnoncrysol.2005.06.008
 17. Saha A, Raj R, and Williamson DL. A Model for the Nanodomains in Polymer-Derived SiCO. *Journal of the American Ceramic Society*. 2006; 89:2188–95. DOI: 10.1111/j.1551-2916.2006.00920.x
 18. Kroll P. Modelling and Simulation of Amorphous Silicon Oxycarbide. *Journal of Materials Chemistry*. 2003; 13:1657–68. DOI: 10.1039/B301389H
 19. Kroll P. Modeling the ‘Free Carbon’ Phase in Amorphous Silicon Oxycarbide. *Journal of Non-Crystalline Solids*. *Proceedings of the International Conference on Non-Crystalline Materials (CONCIM) 2005* May 1; 351:1121–6. DOI: 10.1016/j.jnoncrysol.2005.01.010
 20. Kroll P. Searching Insight into the Atomistic Structure of SiCO Ceramics. *Journal of Materials Chemistry*. 2010; 20:10528–34. DOI: 10.1039/C0JM01583K
 21. Duin ACT van, Dasgupta S, Lorant F, and Goddard WA. ReaxFF: A Reactive Force Field for Hydrocarbons. *The Journal of Physical Chemistry A*. 2001 Oct 1; 105:9396–409. DOI: 10.1021/jp004368u
 22. Newsome DA, Sengupta D, Foroutan H, Russo MF, and Duin ACT van. Oxidation of Silicon Carbide by O₂ and H₂O: A ReaxFF Reactive Molecular Dynamics Study, Part I. *The Journal of Physical Chemistry C*. 2012 Aug 2; 116:16111–21. DOI: 10.1021/jp306391p
 23. Soria FA, Zhang W, Paredes-Olivera PA, van Duin AdriCT, and Patrito EM. Si/C/H ReaxFF Reactive Potential for Silicon Surfaces Grafted with Organic Molecules. *The Journal of Physical Chemistry C*. 2018 Oct 18; 122:23515–27. DOI: 10.1021/acs.jpcc.8b07075
 24. Gao H, Wang H, Zhao Z, Niu M, Su L, and Wei Y. Reactive Dynamics Simulation Study on the Pyrolysis of Polymer Precursors To Generate Amorphous Silicon Oxycarbide Structures. *The Journal of Physical Chemistry C*. 2018 Mar 15; 122:5767–73. DOI: 10.1021/acs.jpcc.7b12287
 25. Ponomarev I, Duin ACT van, and Kroll P. Reactive Force Field for Simulations of the Pyrolysis of Polysiloxanes into Silicon Oxycarbide Ceramics. *The Journal of Physical Chemistry C*. 2019 Jul 11; 123:16804–12. DOI: 10.1021/acs.jpcc.9b03810
 26. Khaliullin RZ, Eshet H, Kühne TD, Behler J, and Parrinello M. Graphite-Diamond Phase Coexistence Study Employing a Neural-Network Mapping of the Ab Initio Potential Energy Surface. *Physical Review B*. 2010 Mar 18; 81:100103. DOI: 10.1103/PhysRevB.81.100103
 27. Deringer VL and Csányi G. Machine Learning Based Interatomic Potential for Amorphous Carbon. *Physical Review B*. 2017 Mar

- 3; 95:094203. DOI: 10.1103/PhysRevB.95.094203
28. Wen M and Tadmor EB. Hybrid Neural Network Potential for Multilayer Graphene. *Physical Review B*. 2019 Nov 18; 100:195419. DOI: 10.1103/PhysRevB.100.195419
 29. Caro MA. Optimizing Many-Body Atomic Descriptors for Enhanced Computational Performance of Machine Learning Based Interatomic Potentials. *Physical Review B*. 2019 Jul 30; 100:024112. DOI: 10.1103/PhysRevB.100.024112
 30. Rowe P, Deringer VL, Gasparotto P, Csányi G, and Michaelides A. An Accurate and Transferable Machine Learning Potential for Carbon. *The Journal of Chemical Physics*. 2020 Jul 21; 153:034702. DOI: 10.1063/5.0005084
 31. Shaidu Y, Küçükbenli E, Lot R, Pellegrini F, Kaxiras E, and Gironcoli S de. A Systematic Approach to Generating Accurate Neural Network Potentials: The Case of Carbon. *npj Computational Materials*. 2021 Apr 14; 7(1):1–13. DOI: 10.1038/s41524-021-00508-6
 32. Wang J, Shen H, Yang R, Xie K, Zhang C, Chen L, Ho KM, Wang CZ, and Wang S. A Deep Learning Interatomic Potential Developed for Atomistic Simulation of Carbon Materials. *Carbon*. 2022 Jan 1; 186:1–8. DOI: 10.1016/j.carbon.2021.09.062
 33. Qamar M, Mrovec M, Lysogorskiy Y, Bochkarev A, and Drautz R. Atomic Cluster Expansion for Quantum-Accurate Large-Scale Simulations of Carbon. *Journal of Chemical Theory and Computation*. 2023 Jun 22. DOI: 10.1021/acs.jctc.2c01149
 34. Bartók AP, Kermode J, Bernstein N, and Csányi G. Machine Learning a General-Purpose Interatomic Potential for Silicon. *Physical Review X*. 2018 Dec 14; 8:041048. DOI: 10.1103/PhysRevX.8.041048
 35. Qian X, Peng S, Li X, Wei Y, and Yang R. Thermal Conductivity Modeling Using Machine Learning Potentials: Application to Crystalline and Amorphous Silicon. *Materials Today Physics*. 2019 Aug 1; 10:100140. DOI: 10.1016/j.mtphys.2019.100140
 36. Yokoi T, Noda Y, Nakamura A, and Matsunaga K. Neural-Network Interatomic Potential for Grain Boundary Structures and Their Energetics in Silicon. *Physical Review Materials*. 2020 Jan 29; 4:014605. DOI: 10.1103/PhysRevMaterials.4.014605
 37. George J, Hautier G, Bartók AP, Csányi G, and Deringer VL. Combining Phonon Accuracy with High Transferability in Gaussian Approximation Potential Models. *The Journal of Chemical Physics*. 2020 Jul 28; 153:044104. DOI: 10.1063/5.0013826
 38. Hamedani A, Byggmästar J, Djurabekova F, Alahyarizadeh G, Ghaderi R, Minuchehr A, and Nordlund K. Insights into the Primary Radiation Damage of Silicon by a Machine Learning Interatomic Potential. *Materials Research Letters*. 2020 Oct 2; 8:364–72. DOI: 10.1080/21663831.2020.1771451
 39. Lysogorskiy Y, Oord C van der, Bochkarev A, Menon S, Rinaldi M, Hammerschmidt T, Mrovec M, Thompson A, Csányi G, Ortner C, and Drautz R. Performant Implementation of the Atomic Cluster Expansion (PACE) and Application to Copper and Silicon. *npj Computational Materials*. 2021 Dec; 7:97. DOI: 10.1038/s41524-021-00559-9
 40. Novikov IS and Shapeev AV. Improving Accuracy of Interatomic Potentials: More Physics or More Data? A Case Study of Silica. *Materials Today Communications*. 2019 Mar 1; 18:74–80. DOI: 10.1016/j.mtcomm.2018.11.008
 41. Balyakin IA, Rempel SV, Ryltsev RE, and Rempel AA. Deep Machine Learning Interatomic Potential for Liquid Silica. *Physical Review E*. 2020 Nov 23; 102:052125. DOI: 10.1103/PhysRevE.102.052125
 42. Kobayashi K, Nagai Y, Itakura M, and Shiga M. Self-Learning Hybrid Monte Carlo Method for Isothermal–Isobaric Ensemble: Application to Liquid Silica. *The Journal of Chemical Physics*. 2021 Jul 21; 155:034106. DOI: 10.1063/5.0055341
 43. Erhard LC, Rohrer J, Albe K, and Deringer VL. A Machine-Learned Interatomic Potential for Silica and Its Relation to Empirical Models. *npj Computational Materials*. 2022 Dec; 8:90. DOI: 10.1038/s41524-022-00768-w
 44. Kutzhanov MK, Matveev AT, Kvashnin DG, Corthay S, Kvashnin AG, Konopatsky AS, Bondarev AV, Arkharova NA, and Shtansky DV. Al/SiC Nanocomposites with Enhanced Thermomechanical Properties Obtained from Microwave Plasma-Treated Nanopowders. *Materials Science and Engineering: A*. 2021 Sep 8; 824:141817. DOI: 10.1016/j.msea.2021.141817
 45. Liu Y, Wang H, Guo L, Yan Z, Zheng J, Zhou W, and Xue J. Deep Learning Interatomic Potential for Irradiation Damage in 3C-SiC. 2023 May 30. DOI: 10.48550/arXiv.2305.19516. arXiv: 2305.19516 [cond-mat]. Available from: <http://arxiv.org/abs/2305.19516> [Accessed on: 2023 Jun 26]. preprint
 46. Novikov IS, Gubaev K, Podryabinkin EV, and Shapeev AV. The MLIP Package: Moment Tensor Potentials with MPI and Ac-

- Machine Learning. *Machine Learning: Science and Technology*. 2021 Jan; 2:025002. DOI: 10.1088/2632-2153/abc9fe
47. Lysogorskiy Y, Bochkarev A, Mrovec M, and Drautz R. Active Learning Strategies for Atomic Cluster Expansion Models. *Physical Review Materials*. 2023 Apr 12; 7:043801. DOI: 10.1103/PhysRevMaterials.7.043801
 48. Erhard LC, Rohrer J, Albe K, and Deringer VL. Modelling Atomic and Nanoscale Structure in the Silicon-Oxygen System through Active Machine Learning. 2023 Sep 7. DOI: 10.48550/arXiv.2309.03587. arXiv: 2309.03587 [cond-mat]. Available from: <http://arxiv.org/abs/2309.03587> [Accessed on: 2023 Sep 13]. preprint
 49. Hjorth Larsen A, Jørgen Mortensen J, Blomqvist J, Castelli IE, Christensen R, Dułak M, Friis J, Groves MN, Hammer B, Hargus C, Hermes ED, Jennings PC, Bjerre Jensen P, Kermode J, Kitchin JR, Leonhard Kolsbjerg E, Kubal J, Kaasbjerg K, Lysgaard S, Bergmann Maronsson J, Maxson T, Olsen T, Pastewka L, Peterson A, Rostgaard C, Schiøtz J, Schütt O, Strange M, Thygesen KS, Vegge T, Vilhelmsen L, Walter M, Zeng Z, and Jacobsen KW. The Atomic Simulation Environment—a Python Library for Working with Atoms. *Journal of Physics: Condensed Matter*. 2017 Jul 12; 29:273002. DOI: 10.1088/1361-648X/aa680e
 50. Jain A, Ong SP, Hautier G, Chen W, Richards WD, Dacek S, Cholia S, Gunter D, Skinner D, Ceder G, and Persson KA. Commentary: The Materials Project: A Materials Genome Approach to Accelerating Materials Innovation. *APL Materials*. 2013 Jul; 1:011002. DOI: 10.1063/1.4812323
 51. Rohrer J, Vrankovic D, Cupid D, Riedel R, Seifert HJ, Albe K, and Graczyk-Zajac M. Si- and Sn-containing SiOCN-based Nanocomposites as Anode Materials for Lithium Ion Batteries: Synthesis, Thermodynamic Characterization and Modeling. *International Journal of Materials Research*. 2017 Nov 10; 108:920–32. DOI: 10.3139/146.111517
 52. Šić E, Rohrer J, Ricohermoso EI, Albe K, Ionescu E, Riedel R, Breitzke H, Gutmann T, and Buntkowsky G. SiCO Ceramics as Storage Materials for Alkali Metals/Ions: Insights on Structure Moieties from Solid-State NMR and DFT Calculations. *ChemSusChem*. n/a:e202202241. DOI: 10.1002/cssc.202202241
 53. Martínez L, Andrade R, Birgin EG, and Martínez JM. PACKMOL: A package for building initial configurations for molecular dynamics simulations. *Journal of Computational Chemistry*. 2009; 30:2157–64. DOI: 10.1002/jcc.21224
 54. Martínez JM and Martínez L. Packing Optimization for Automated Generation of Complex System’s Initial Configurations for Molecular Dynamics and Docking. *Journal of Computational Chemistry*. 2003; 24:819–25. DOI: 10.1002/jcc.10216
 55. Wen Q, Yu Z, and Riedel R. The Fate and Role of in Situ Formed Carbon in Polymer-Derived Ceramics. *Progress in Materials Science*. 2020 Apr 1; 109:100623. DOI: 10.1016/j.pmatsci.2019.100623
 56. Delverdier O, Monthieux M, Mocaer D, and Paillet R. Thermal Behavior of Polymer-Derived Ceramics. I. Si-C and Si-C-O Systems from Both Commercial and New Polycarbosilane (PCS) Precursors. *Journal of the European Ceramic Society*. 1993 Jan 1; 12:27–41. DOI: 10.1016/0955-2219(93)90068-3
 57. Pantano CG, Singh AK, and Zhang H. Silicon Oxycarbide Glasses. *Journal of Sol-Gel Science and Technology*. 1999 Mar 1; 14:7–25. DOI: 10.1023/A:1008765829012
 58. Podryabinkin EV and Shapeev AV. Active Learning of Linearly Parametrized Interatomic Potentials. *Computational Materials Science*. 2017 Dec 1; 140:171–80. DOI: 10.1016/j.commatsci.2017.08.031
 59. Bochkarev A, Lysogorskiy Y, Menon S, Qamar M, Mrovec M, and Drautz R. Efficient Parametrization of the Atomic Cluster Expansion. *Physical Review Materials*. 2022 Jan 24; 6:013804. DOI: 10.1103/PhysRevMaterials.6.013804
 60. Kresse G, Furthmüller J, and Hafner J. Theory of the Crystal Structures of Selenium and Tellurium: The Effect of Generalized-Gradient Corrections to the Local-Density Approximation. *Physical Review B*. 1994 Nov 1; 50:13181–5. DOI: 10.1103/PhysRevB.50.13181
 61. Kresse G and Furthmüller J. Efficiency of Ab-Initio Total Energy Calculations for Metals and Semiconductors Using a Plane-Wave Basis Set. *Computational Materials Science*. 1996 Jul 1; 6:15–50. DOI: 10.1016/0927-0256(96)00008-0
 62. Kresse G and Furthmüller J. Efficient Iterative Schemes for Ab Initio Total-Energy Calculations Using a Plane-Wave Basis Set. *Physical Review B*. 1996 Oct 15; 54:11169–86. DOI: 10.1103/PhysRevB.54.11169
 63. Kresse G and Joubert D. From Ultrasoft Pseudopotentials to the Projector Augmented-Wave Method. *Physical Review B*. 1999 Jan 15; 59:1758–75. DOI: 10.1103/PhysRevB.59.1758
 64. Sun J, Ruzsinszky A, and Perdew JP. Strongly Constrained and Appropriately Normed Semilocal Density Functional. *Physi-*

- cal Review Letters. 2015 Jul 14; 115:036402. DOI: 10.1103/PhysRevLett.115.036402
65. Thompson AP, Aktulga HM, Berger R, Bolintineanu DS, Brown WM, Crozier PS, Veld PJ in, Kohlmeyer A, Moore SG, Nguyen TD, Shan R, Stevens MJ, Tranchida J, Trott C, and Plimpton SJ. LAMMPS - a Flexible Simulation Tool for Particle-Based Materials Modeling at the Atomic, Meso, and Continuum Scales. *Computer Physics Communications*. 2022 Feb 1; 271:108171. DOI: 10.1016/j.cpc.2021.108171
 66. Renlund GM, Prochazka S, and Doremus RH. Silicon Oxycarbide Glasses: Part II. Structure and Properties. *Journal of Materials Research*. 1991 Dec 1; 6:2723–34. DOI: 10.1557/JMR.1991.2723
 67. Sorarù GD, Dallapiccola E, and D’Andrea G. Mechanical Characterization of Sol–Gel-Derived Silicon Oxycarbide Glasses. *Journal of the American Ceramic Society*. 1996; 79:2074–80. DOI: 10.1111/j.1151-2916.1996.tb08939.x
 68. Walter S, Soraru GD, Bréquel H, and Enzo S. Microstructural and Mechanical Characterization of Sol Gel-Derived Si–O–C Glasses. *Journal of the European Ceramic Society*. 2002 Dec 1; 22:2389–400. DOI: 10.1016/S0955-2219(01)00537-4
 69. Moysan C, Riedel R, Harshe R, Rouxel T, and Augereau F. Mechanical Characterization of a Polysiloxane-Derived SiOC Glass. *Journal of the European Ceramic Society*. 2007 Jan 1; 27:397–403. DOI: 10.1016/j.jeurceramsoc.2006.01.016
 70. Stabler C, Celarie F, Rouxel T, Limbach R, Wondraczek L, Riedel R, and Ionescu E. Effect of Composition and High-Temperature Annealing on the Local Deformation Behavior of Silicon Oxycarbides. *Journal of the European Ceramic Society*. 2019 Jul; 39:2287–96. DOI: 10.1016/j.jeurceramsoc.2019.02.024
 71. Sorarù GD, Kundanati L, Santhosh B, and Pugno N. Influence of Free Carbon on the Young’s Modulus and Hardness of Polymer-Derived Silicon Oxycarbide Glasses. *Journal of the American Ceramic Society*. 2019; 102:907–13. DOI: 10.1111/jace.16131
 72. Ong SP, Richards WD, Jain A, Hautier G, Kocher M, Cholia S, Gunter D, Chevrier VL, Persson KA, and Ceder G. Python Materials Genomics (Pymatgen): A Robust, Open-Source Python Library for Materials Analysis. *Computational Materials Science*. 2013 Feb 1; 68:314–9. DOI: 10.1016/j.commatsci.2012.10.028
 73. Inaba S, Fujino S, and Morinaga K. Young’s Modulus and Compositional Parameters of Oxide Glasses. *Journal of the American Ceramic Society*. 1999; 82:3501–7. DOI: 10.1111/j.1151-2916.1999.tb02272.x
 74. Haseen S and Kroll P. Analyzing the Effect of Composition, Density, and the Morphology of the “Free” Carbon Phase on Elastic Moduli in Silicon Oxycarbide Ceramics. *Journal of the European Ceramic Society*. 2023 Apr 1; 43:1432–41. DOI: 10.1016/j.jeurceramsoc.2022.11.025
 75. Leimeroth N, Rohrer J, and Albe K. Potential and Training Data for ‘Structure-Property Relations of Silicon Oxycarbides Studied Using a Novel Machine Learning Interatomic Potential’. DOI: 10.5281/zenodo.10131450